

Prototype of a segmented scintillator detector for particle flux measurements on spacecraft

Egor Stadnichuk^{1,2} Tatyana Abramova¹ Mikhail Zelenyi^{1,2,3} Alexander Izvestnyy² Alexander Nozik^{1,2} Vladimir Palmin^{1,2} Ivan Zimovets³

¹*Moscow Institute of Physics and Technology (National Research University) - MIPT, 1 "A" Kerchenskaya st., Moscow, Russia, 117303*

²*Institute for Nuclear Research of the Russian Academy of Sciences (INR RAS), Prospekt 60-letiya Oktyabrya 7a, Moscow, Russia, 117312*

³*Space Research Institute of the Russian Academy of Sciences (IKI RAS), 84/32 Profsoyuznaya st., Moscow, Russia, 117997*

E-mail: yegor.stadnichuk@phystech.edu

ABSTRACT: In this paper we introduce a laboratory prototype of a solar energetic particle (SEP) detector which will operate along with other space-based instruments to give us more insight into the SEP physics. The instrument is designed to detect protons and electrons with kinetic energies from 10 to 100 MeV and from 1 to 10 MeV respectively. The detector is based on a scintillation cylinder divided into separated disks to get more information about detected particles. Scintillation light from isolated segments is collected by optical fibers and detected with silicon photo-multipliers (SiPM). The work contains the result of laboratory testing of the detector prototype. The detector channels were calibrated, energy resolution for every channel was obtained. Moreover, we present an advanced integral data acquisition and analysis technique based on Bayesian statistics, which will allow operation even during SEP events with very large fluxes.

The work is motivated by the need for better measurement tools to study acceleration and transport of SEP in the heliosphere as well as by the need for monitoring tool to mitigate radiation hazard for equipment and people in space.

Contents

1	Introduction	1
2	Detector response	4
3	The prototype detector	5
4	Shape-based signal processing	8
5	Detector calibration	8
6	Fast signal processing	9
7	Integral mode data analysis	11
8	Conclusion	15

1 Introduction

The Sun is a magnetically active star. As a result of the processes of transformation of free magnetic energy occurring in active regions in the solar atmosphere, populations of solar energetic particles (SEPs) or solar cosmic rays (SCRs) with energies ranging from tens of keV to several GeV sporadically appear in the interplanetary (IP) medium (e.g., [10, 15]). Due to the composition of the chemical elements of the Sun, the most numerous are populations of energetic electrons and protons. Among SEPs, there are also heavier nuclei from He to Fe, but in much smaller quantities.

According to the modern paradigm [10, 17], the SEP events (SEPEs) are divided into two main groups: 1) impulsive events associated with coronal jets or impulsive solar flares, 2) gradual events with long-duration eruptive flares accompanied by fast ($v > \approx 1000$ km/s) coronal mass ejections (CMEs) and related large-scale shock waves. Usually impulsive SEPEs last several tens of minutes or a few hours and accelerate electrons predominately, whereas gradual SEPEs can last several days, manifesting themselves in the form of SEP radiation storms in the IP medium. Distinctive features of impulsive SEPEs are: fast-drifting type III radio bursts (associated with beams of accelerated electrons propagating through plasma of the corona and IP medium), a relatively narrow (up to a few tens of degrees) cone of spread in the IP medium and good magnetic connection with a parent flare region on the Sun, the increased by $\sim 10^3 - 10^4$ ratio of $^3\text{He}/^4\text{He}$, the increased by ~ 10 ratio of Fe/O ions relative to the nominal coronal values, the ionization state of Fe around 2. Gradual SEPEs are usually accompanied by slow-drifting type II radio bursts (associated with the plasma mechanism of radiation on a propagating shock wave), they are rich in protons, the average Fe/O ratio is of the order of 0.1, the ionization state of Fe is around 14, and wide particle spread in the heliographic longitudes (up to 180 degrees and even higher) and latitudes.

It is believed, within the framework of the modern paradigm, that the properties of impulsive SEPEs can be explained by the relatively faster (minutes) acceleration of charged particles in flare regions on the Sun at relatively low altitudes up to 50-100 Mm above the photosphere as a result of magnetic reconnection, whereas in gradual SEPEs particles can be accelerated for long time (tens of hours) by a shock wave, moving away from the Sun and expanding in the IP medium. In periods of high solar activity, when events occur close in time to each other (within several hours), mixed or hybrid SEPEs also occur [8].

Despite the widespread acceptance of the modern paradigm, the fundamental problem of SEPs/SCRs is still far from a complete solution. Some important questions still remain. For example: how exactly are particles accelerated in impulsive and long-duration solar flares, what is the role of magnetic reconnection and eruptive magnetic flux ropes in particle acceleration and escape from the corona, where and how exactly do particles make longitude-latitudinal transport, how and where seed populations of particles are formed for further acceleration at shock waves. Moreover, the modern paradigm has an alternative. Some researchers believe that in all SEPEs, both in impulsive and gradual ones, solar flares play a key role in the acceleration of electrons and protons, and coronal/IP shocks play only a secondary role (e.g., [14, 20]). It is suggested that there are two phases of acceleration in solar flares. In the first phase, electrons are mainly accelerated to relatively low energies of ~ 100 keV, and in the second phase, simultaneous long-term acceleration of electrons and protons to relativistic energies occurs. The importance of simultaneous measurements of solar energetic electrons and protons in a wide range of energies for understanding the mechanisms of their acceleration is emphasized in [19]. A reliable determination of the energy spectra of electrons and protons is important for determining their acceleration and transport mechanisms (e.g., [15]). Since electrons are lighter particles, they have much higher speeds at the same energies as protons. With simultaneous injection, relativistic electrons arrive at a distant observer before protons. Based on this idea, a method of short-term (from a few to tens of minutes) prediction of the arrival of solar energetic protons by analyzing the arrival of energetic electrons was proposed in [16].

Besides the importance of studying SEPs from the point of view of solving the fundamental problem of SEPs/SCRs, the detection and investigation of SEPs is also of great practical importance. The “heavy” component of SEPs - protons and various ions up to Fe with energies above ~ 50 MeV - has the most serious negative effect on spacecraft, on its electronic components, and on astronauts on board (e.g., [10, 15]). Penetrating into the magnetosphere, especially in high-latitude regions with a “quasi-open” geometry of magnetic field lines, SEPs can affect the Earth’s ionosphere and atmosphere, causing radio interference, interruptions in satellite orientation and navigation, as well as creating increased doses of radiation absorbed by pilots and passengers of airliners. Relativistic electrons capable of penetrating deep enough under the lining of spacecraft can cause the volume electrification effect associated with the formation of deep dielectric charging [3, 9]. If the fluxes of energetic electrons are large enough for a long time, then the charge does not have time to dissolve, reaches critical values and causes micro-breakdowns, which lead to disruption of the on-board electronics.

SEPs with energies up to a few hundred MeV do not penetrate down to the Earth’s surface through the magnetosphere and atmosphere. They can be detected only with the help of instruments installed on board spacecraft. Many SEP instruments have been developed and launched into space (e.g., [21]). Of the latter, there are the Integrated Science Investigation of the Sun (ISIS) suit of

detectors aboard Parker Solar Probe [11] and the Energetic Particle Detector (EPD) instrument aboard Solar Orbiter [18]. Typically, such instruments are sets of charged particle telescopes - multilayer assemblies of semiconductor detectors. Sometimes separate thick scintillation detectors are added to the semiconductor detector system, the light signal from which is taken by means of photoelectronic multipliers (PMTs). These scintillation detectors are used as calorimeters, in which the bulk of the energy of the measured particle is released, as well as an anti-coincidence shielding. The use of multilayer scintillation detectors was previously unjustified in SEP telescopes due to the bulkiness of the PMTs used and the relatively lower energy resolution. However, the situation has changed in recent years, as it has become possible to replace bulky traditional PMTs with significantly more compact silicon photomultipliers - SiPMs (e.g., [4, 5]).

In this article, we present the results of the development and calibration of a laboratory prototype of a SEP detector-telescope (electrons with energies $\sim 1 - 10$ MeV, protons $\sim 10 - 100$ MeV), based on a multi-layer system of plastic scintillation detectors with compact SiPMs.

Detector construction

There are several requirements for the telescope. Firstly, it must have a good energy resolution (at least $\Delta E/E \approx 10 - 15\%$). Secondly, it should also work at high particle fluxes to measure the spectrum during intense SEPEs (up to $\sim 10^6 - 10^7$ particles per second). Thirdly, to use the detector in space, it must have small mass-dimensional characteristics. In order to optimize the detector geometry, we used Geant4 simulation. The results of the simulation are presented in [22].

The optimal geometry of the detector strongly depends on the physics of radiation passing through matter. Firstly, the length of the scintillator detector is defined by the maximum penetration of particles of interest. For 10 MeV electrons and 100 MeV protons the penetration through a scintillator is similar - about 7 cm. The final prototype length of 8 cm reasonably covers the energy region. The width of the detector is defined by the following condition: detector should detect most of the electromagnetic cascade generated by detected particles. According to the simulation, the width of the avalanche even for the electrons does not exceed 3 cm in most cases. Thus the basic shape of the detector is a cylinder with a width of 8 cm and diameter 3 cm.

The primary feature of the detector is its segmentation. A detector segment is a scintillator disk of variable height. The division makes it possible to obtain not only total energy deposition of a particle, but also its dependence on penetration depth. This information allows to significantly increase precision of energy reconstruction especially for protons, for which the shape of energy deposition has a well known peculiarity - Bragg peak (figure 1). The analysis of the loss function shape also allows to distinguish between electrons and protons with the same total energy deposition, because they have different per-segment deposition.

The height of the disk should balance two factors. On the one hand, the thinner detector segments are, the more accurately loss function is measured, so we can get better precision. But, on the other hand, the thinner the cylinder, the less light one will get from energy loss in it. The number of detected photons directly affects the energy resolution of a single segment. Also there is a physical detection threshold for preamplifiers. Moreover, a lot of disks requires more complicated and more massive electronics resulting in increasing the device mass, power consumption and telemetry volume. For the prototype we decided to use disks of 0.4 cm height, which according

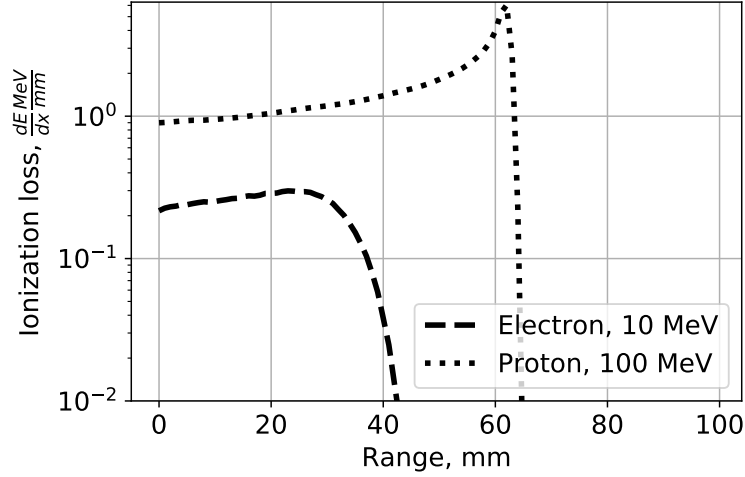


Figure 1: Proton and electron loss functions in a plastic scintillator. Protons have strongly marked Bragg peak. Firstly, it makes them distinguishable from electrons. Secondly, proton energy can be judged by position of the Bragg peak.

to simulations, provides reasonable balance between number of measurement channels and loss function measurement precision. To cover the length of 8 cm, we need 20 such disks, which also means 20 channels of measuring electronics.

Light from disks is transported via optical fiber to silicon photo-multiplier detectors (SiPM). Detectors are attached to front-end electronics with integrated preamplifiers and automatically adjusted power supply for bias voltage. The output of the front-end electronics is processed by a back-end amplifier and digitizer.

2 Detector response

A charged particle, when passing through a scintillator, loses energy, part of which is converted into visible light. Visible light is then detected by a photodetector. The number of registered photons is directly proportional to the energy lost by the particle inside the scintillator. When passing through a scintillator, charged particles have a characteristic function of energy loss per unit path length. For protons, for example, the loss function has a Bragg peak, the spatial position of which can be used to precisely determine the proton energy (figure 1). On the other hand, electron loss function does not possess such significant peak. Though with worse precision, electron energy is also resolvable from the curve. Moreover, the difference in proton and electron loss curve shapes allows one to distinguish these particles from each other.

The detector is a cylinder segmented into several scintillation layers (disks). Such a design makes it possible to restore the particle loss function depending on the penetration depth. Thus, in addition to information about the total energy release of the particle, the detector receives information about the profile of its loss curve ($\Delta E/\Delta x$), which allows one to determine the type of particle and its energy with good resolution.

By design, the detector should be able to operate in two modes:

- Single-particle mode. This mode could be used when the total count rate is relatively low (up to 10^5 particles per second). In this case, it is possible to analyze each particle separately. The energy and type of particle is restored from its loss curve by the method of maximum likelihood.
- Integral mode. In this mode, the specific energy deposition of each particle is not measured, instead the total light yield is integrated in each segment over fixed time. Information on the spectrum of particles is reconstructed from the total curve of their losses obtained during the exposure. The spectrum is obtained by solving the inverse problem by the Turchin regularization method [7], or the least squares method, or by fitting the spectrum of particles. The result of reconstructing the spectrum of particles in the integral mode on model data by the method of statistical regularization is presented in section 7.

3 The prototype detector

The experimental prototype of the detector developed in INR RAS is a cylinder composed of 20 scintillation disks (figure 2, figure 3). A polystyrene-based material is used as a scintillator. The diameter of a disk is 3 cm, the thickness is 0.4 cm. Each scintillator is wrapped in a reflective material - Tyvek, produced by DuPont company ([1]. It prevents optical cross-talk between channels and, moreover, increases photon detection efficiency. Scintillation light is detected using the Hamamatsu S12575-015P SiPM photodetectors [2].

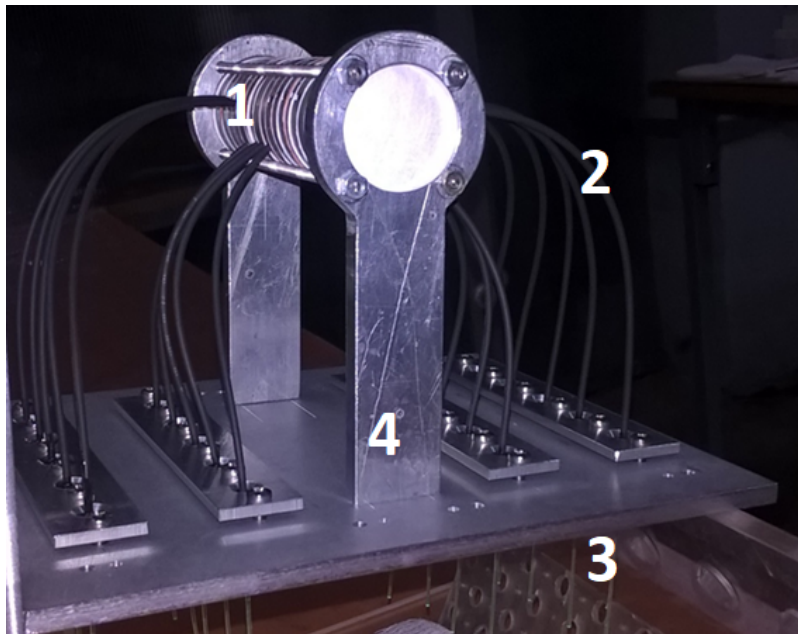


Figure 2: Photo of the detector prototype with the aluminum support structure. 1 - scintillator disks, 2 - optical fibers, wrapped in a black insulating coating, 3 - electronics with SIPMs attaching point, 4 - aluminium stand.



Figure 3: Photo of the detector electronic board with 10 SiPMs installed.

Two ways to register light with the SiPM were considered. The first way is to attach the photodetector directly to the disk. The second method is to collect scintillation light using optical fiber and connect the optical fiber to the photodetector (figure 5). To select the optimal detector disk design the following experiment was conducted. The first and second options for attaching a photo detector were implemented. Then the disks were irradiated with the Sr 90 laboratory beta source. It emits beta electrons with energies up to 1.5 MeV. The received signals were transmitted to a computer using the circuit shown in the (figure 4). The disk signal is determined by the following parameters: the number of photo-electrons and the uniformity of light collection. The number of photo-electrons is a parameter that shows the magnitude of the signal from the segment disk per unit of energy released within the disk by a high-energy particle. The uniformity of the light collection shows how strongly the signal of the detector depends on the point at which the particle enters it. It turned out that a design with a photodetector attached directly to the disk gives a 3 times larger number of photoelectrons compared to the design with optical fiber. However, the second method of attaching the photodetector provides almost complete uniformity of light collection in contrast to the first one. For example, when the SiPM is attached directly to the disk, the signal from a particle that hits the edge of the disk drops more than 2 times compared to the central hit. In the design with optical fiber, the difference between the same signals is 10 – 20%. Since the difference in the number of photoelectrons by 3 times reduces the error only to the root of 3 times, the second design turned out to be more efficient.

Thus, scintillation photons are transmitted to photodetectors by the optical fibres. The design with optical fibers has another significant advantage. It is possible to transport light far enough from the detector cylinder so one could provide additional radiation shielding for SiPMs and the electronics. A photo of the assembled detector layout is shown in figure 2. A photo of one electronic board with 10 SiPMs installed is shown in figure 3. Two identical electronic boards (previously used in hadron calorimeters on accelerator experiments) are attached to the bottom of the breadboard so that optical fibers connect directly to the SiPMs through an optical isolation. All SiPMs are located on a heat-conducting substrate, which makes it possible to equalize their temperature. There is a thermocouple on the electronic board that allows to determine the temperature of the photodetectors. The slow control unit is connected to the electronics, supplying prescribed voltage to the SiPM taking into account its dependence on the temperature.

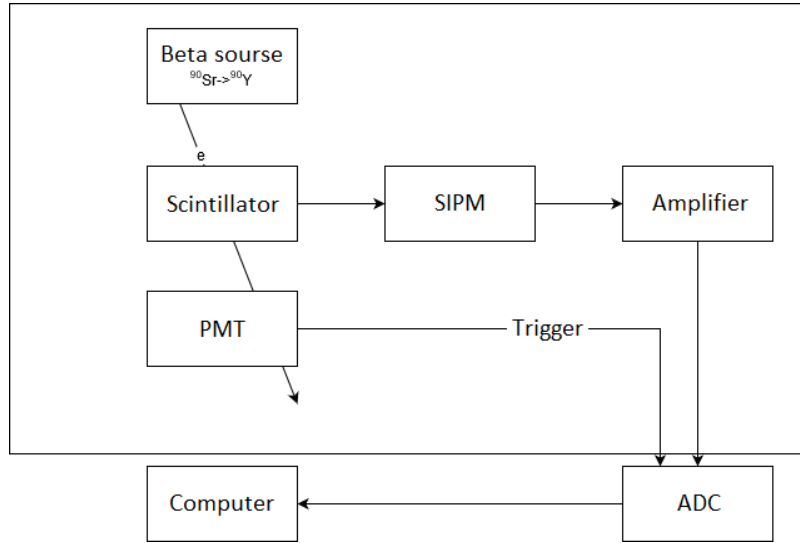


Figure 4: The scheme of a circuit being used for number of photoelectrons measurement.

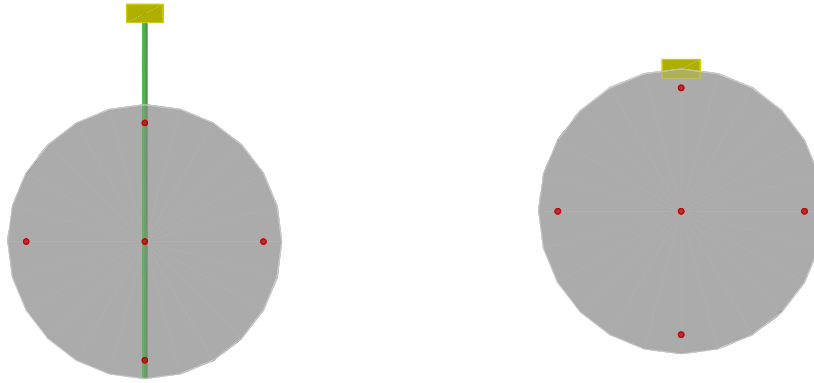


Figure 5: Two ways to collect photons from a scintillator disk. On the left picture - light collection via an optical fiber. On the right picture - direct attachment of a SiPM to the scintillator disk. The way with an optical fiber turned out to be more practical.

The temperature dependence of the optimal voltage to be applied to a SiPM S12575-015P is well-known and described in the documentation [2]. However, in this work, it was verified experimentally. The disk and photodetector system was placed in a thermostat. The disk was irradiated using a laboratory beta source. First, at room temperature, the optimum voltage on a SiPM specified in the documentation was set. The optimal voltage for the room temperature was chosen as 71.5 V. The response of the system to beta radiation was measured. Then, at different temperatures, a voltage was selected so that the response was the same as at room temperature. The temperature dependence of the optimal voltage on the SiPM was obtained (figure 6). With an increase in SiPM's temperature of 1 degree Celsius, it is necessary to increase the voltage by 58.5 mV. It is consistent with the dependence indicated in the documentation of the photodetector, which

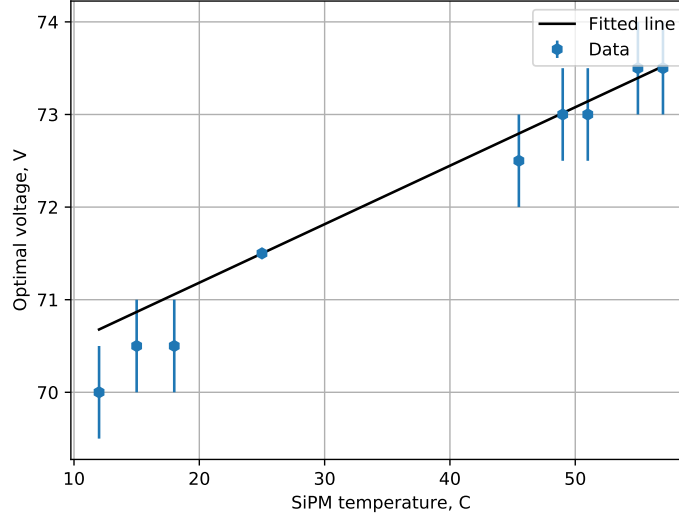


Figure 6: Temperature dependence test result. Optimal SiPM voltage turned out to be consistent with one proposed in the documentation.

says that the voltage must be changed to 60 mV when the temperature changes by 1 degree.

4 Shape-based signal processing

ADC output works in the following way. The data are binary files in which 1028 bits were allocated for each particle. Thus, each passage of a particle through a scintillator disk had a SiPM signal similar to figure 7. However, there were some events with a strong noise. To reduce this error fitting was used. Due to the asymmetry of the tail, the Landau-like distribution ($e^{-(x+e^{-x})}$) was chosen. Its chi-squared distribution shows that there is a reasonable agreement of the fit function with the data.

The following logic chain helps to understand how to get the needful energy information from these graphs. Firstly, the voltage is proportional to the current and the integral of the current is the charge. Meanwhile, the total charge is proportional to the number of photons from the scintillator disk. Finally, the number of photons is proportional to the energy released by a particle. For these reasons, the integral from the peak of the signal is proportional to the energy released by a particle inside the disk. In this way, the released energies were obtained for all events in all disks.

5 Detector calibration

Detector channels were calibrated with atmospheric muons. The calibration was committed in the following steps. First, cosmic muons were detected for one week to gain enough statistics. On the next step, muon signal distribution was derived for every channel. Finally, every experimental distribution was fitted with the theoretical muon signal distribution (figure 8) (section 8). As a result, calibration coefficients for every channel were obtained and, moreover, detector channels energy resolutions were calculated (figures 9 and 10).

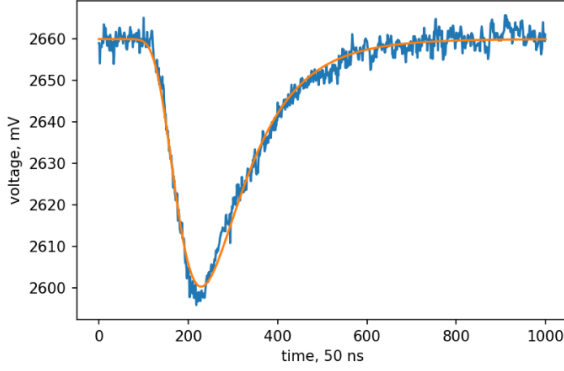


Figure 7: A single event signal fitting with the Landau-like distribution.

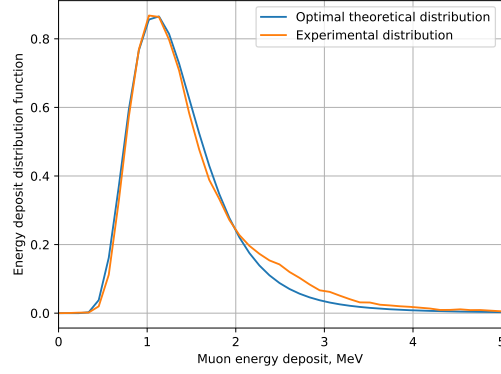


Figure 8: Muon signal in the detector channel 1 distribution fit.

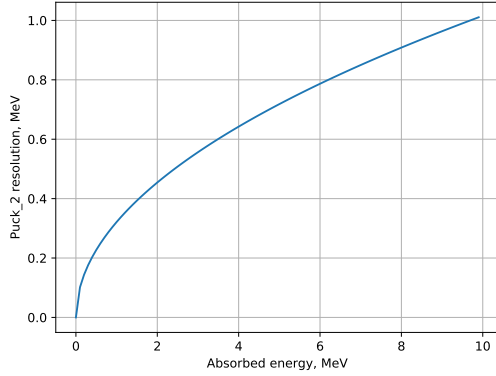


Figure 9: The dependence of the detector channel 2 energy resolution on energy deposit. Dependencies for other channels are similar.

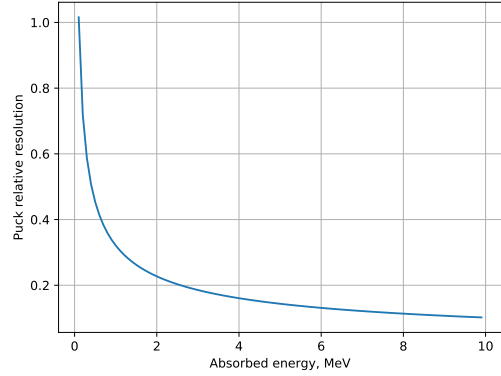


Figure 10: The dependence of the detector channel 2 relative energy resolution on energy deposit. Dependencies for other channels are similar.

Muon signal distribution was fitted in several steps. Firstly, from theoretical distribution it is known that the distribution peak corresponds to vertical muon energy deposit $\varepsilon_0 = 1.02$ MeV. With knowledge about the peak position calibration coefficient was obtained. Secondly, calibrated experimental muon signal distribution was normalized. Finally, normalized and calibrated experimental distribution was fitted with theoretical one. With fitting algorithm channel error was obtained. As a result, each detector channel was calibrated, and for every channel the dependence of the error on the measured energy deposit was received.

6 Fast signal processing

To improve the detection frequency, we considered another type of electronics which gives the width of the SiPM signal at a threshold voltage. And the idea of this method is to restore the integral over the width at a certain voltage. The first step was to check that the integral of a signal is proportional

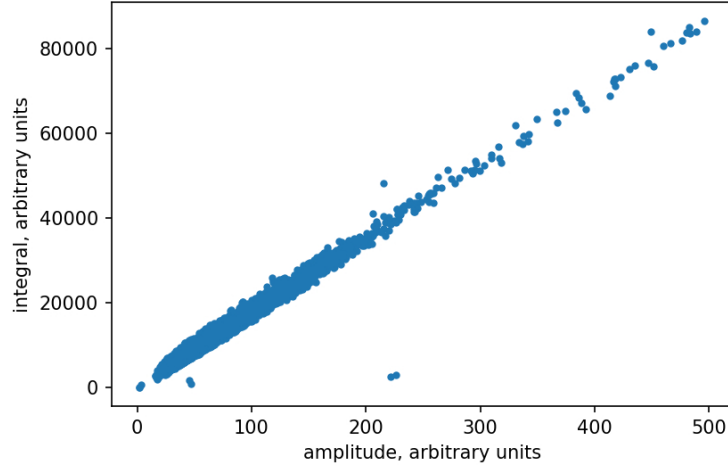


Figure 11: Relationship between integral and amplitude of a signal.

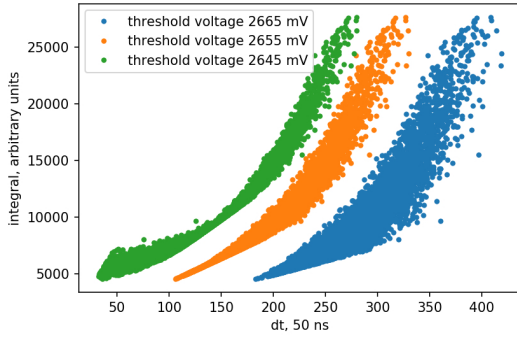


Figure 12: Plots of signal widths at different voltages.

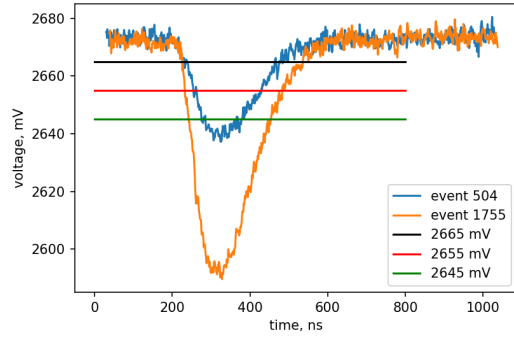


Figure 13: Threshold levels at a signal.

to its amplitude, i.e. the similarity of signals for particles of different energies. As shown at figure 11, there is a linear relationship between the integral and the amplitude.

The next problem was to determine the magnitude of the threshold voltage. First of all, we had to shift signals to one point along time and voltage axes due to a scatter of signal parameters like initial voltage and start of a signal. There is also a relationship between the threshold voltage and scattering of points (figure 12), moreover, there should be the optimum when the scatter is minimum. To understand reasons of this relationship, threshold levels were plotted on the signal (figure 13). It can be seen that the highest level is almost at the end of the signal and the lowest one is almost at the signal minimum level. In addition, it turned out that if we plot the relationship of the width on the voltage then there are intersection points for some events (figure 14).

As a result, a threshold voltage of 2645 mV was chosen, since with it the smallest scatter in the entire sample was achieved and with less values, the voltage turned out to be below the signal minimum. The resulting distribution was fitted by the function $f(x) = a_0 + a_1x + a_3x^3$ (figure 15).

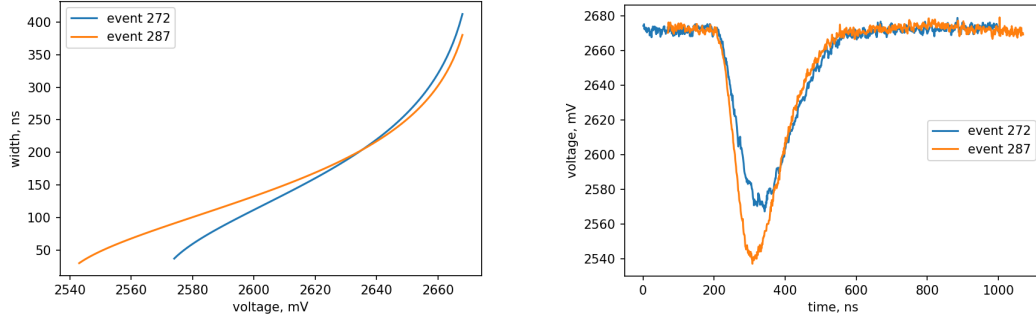


Figure 14: Signals with an intersection point.

Parameter errors are within 1% which allows us to judge the validity of the hypothesis.

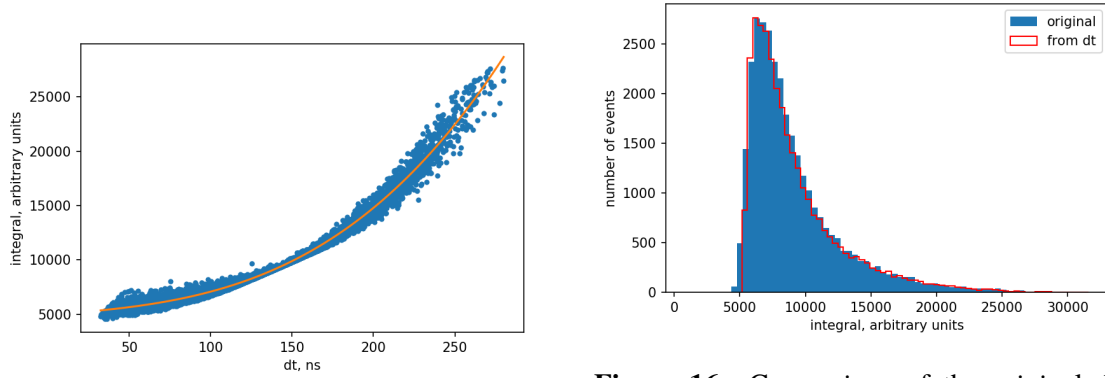


Figure 15: The fitting function

Figure 16: Comparison of the original distribution and the one obtained from the described method.

Finally, to verify that this approach really recovers information about the signal, we compared the distribution of the integrals, the original one obtained directly by calculating the area and the other one obtained from the relationship of the signal width (figure 16). The function described above was applied to a new larger sample that did not contain the original one. The distributions turned out to be very close. Thus, the calibrated detector with new electronics will be able to restore the spectrum of signals for particles of selected energies. At this stage, it can not be said whether it is possible with this method to recover events with higher energies, more than 5 MeV, since the fitting function $f(x)$ is likely to have a completely different shape at high energies. In that the spectrum of signals plays the largest role in further signal processing, it can be judged that this approach lets recover information about particles passing through the detector.

7 Integral mode data analysis

With the increase of particles flux, the detector reaches the maximum count rate for discrete data processing, therefore, the integral mode is required. In the integral mode data is being collected

over a fixed time, then particle energy spectrum is being restored from scintillator energy deposition and previously collected detector calibration data.

Let \vec{f} be the vector of measured energy deposition values from the first to the last disk. Let $\tilde{K}(E, y)$ be the energy deposition of a particle with initial energy E MeV on the coordinate y centimeters of the scintillator (can be approximated from calibration data). Let $\varphi(E)$ be the spectrum of incident cosmic particles. Thus, the problem can be formulated as following: to find the spectrum, the integral equation (7.1) should be solved.

$$f_i = \int_{E_{min}}^{E_{max}} \left(\int_{y_i}^{y_{i+1}} \tilde{K}(E, y) dy \right) \varphi(E) dE \quad (7.1)$$

where y_i - coordinate of the beginning of i -th disk.

Spectrum $\varphi(E)$ can be decomposed in basis $\{T_i(E)\}_{i=1}^I$:

$$\varphi(E) = \sum_{i=1}^I \varphi_i T_i(E) \quad (7.2)$$

where φ_i - i -th coefficient of spectrum decomposition.

Let $K_{i,n}$ be the energy deposition of particles with spectrum $T_i(E)$ in n -th disk.

$$K_{i,n} = \int_{E_{min}}^{E_{max}} \left(\int_{y_n}^{y_{n+1}} \tilde{K}(E, y) dy \right) T_i(E) dE \quad (7.3)$$

As a result, we have linear equation:

$$\vec{f} = K \vec{\varphi} \quad (7.4)$$

Both forms of the problem (7.1) and (7.4) appear to be ill-posed, so they require special solution techniques. One of the possible ways to do it is Turchin statistical regularisation [6, 7]. The concept of this method is that in physical processes almost all spectra are relatively smooth. Adding information of function smoothness, one can solve equation 7.4 correctly and find particles spectrum $\varphi(E)$.

A solution of the equation 7.4 can be found as

$$\vec{\varphi}_{opt} = E[\vec{\varphi}|\vec{f}] = \int \vec{\varphi} P(\vec{\varphi}|\vec{f}) d\vec{\varphi} \quad (7.5)$$

By Bayes' theorem:

$$P(\vec{\varphi}|\vec{f}) = \frac{P(\vec{\varphi})P(\vec{f}|\vec{\varphi})}{\int d\vec{\varphi} P(\vec{\varphi})P(\vec{f}|\vec{\varphi})} \quad (7.6)$$

Every arbitrary distribution $P(\varphi)$ can be used as a prior information about $\varphi(E)$. For instance, we will use information that the $\varphi(E)$ function is relatively smooth. Let Ω be the matrix of average values of the second derivatives

$$\Omega_{ij} = \int_{E_{min}}^{E_{max}} \frac{d^2 T_i(x)}{dx^2} \frac{d^2 T_j(x)}{dx^2} dx \quad (7.7)$$

We express smoothness by parameter α

$$\alpha \int (\vec{\varphi}, \Omega \vec{\varphi}) P(\vec{\varphi}) d\vec{\varphi} = 1 \quad (7.8)$$

This condition should bring as little information about the solution as possible, it means that information entropy has a minimum value

$$\int P(\vec{\varphi}) \ln P(\vec{\varphi}) d\vec{\varphi} \rightarrow \min \quad (7.9)$$

The solution to this problem is a parametric distribution:

$$P(\vec{\varphi}) \sim \exp -\frac{1}{2}(\vec{\varphi}, \alpha\Omega\vec{\varphi}) \quad (7.10)$$

The regularization parameter α can be chosen arbitrarily.

Measured value \vec{f} can have arbitrary distribution, but usually when measuring physical quantities, we have values that are distributed according to the normal distribution

$$P(\vec{f}|\varphi) = \frac{1}{(2\pi)^{N/2}\sqrt{\det \Sigma}} \exp -\frac{1}{2}(\vec{f} - K\vec{\varphi})^T \Sigma^{-1}(\vec{f} - K\vec{\varphi})$$

The product of the a prior distribution and the distribution of the measured quantity has the form of a multidimensional normal distribution. That allows to find $\vec{\varphi}$ and covariance matrix analytically

$$\begin{aligned} \vec{\varphi}_{opt} &= (K^T \Sigma^{-1} K + \alpha\Omega)^{-1} K^T \Sigma^{-1T} \vec{f} \\ cov &= (K^T \Sigma^{-1} K + \alpha\Omega)^{-1} \end{aligned}$$

If the quantity \vec{f} has a distribution other than normal, then the analytical solution is not always easy to find. In that case we should find mode, expectation and dispersion of the distribution using Monte-Carlo techniques.

Knowing the coefficients of the basis and the covariance matrix of the vector, we can find the spectrum functions $\varphi(E)$ at any point lying between E_{min} and E_{max} :

$$\varphi(E) = \sum_{m=1}^M \varphi_m T_m(E)$$

and the error in calculating the spectrum at this point:

$$\delta\varphi(E) = \sqrt{\vec{T}^T(E) \cdot cov \cdot \vec{T}(E)},$$

where $\vec{T}(E)$ - vector of values of basis functions at the point E .

As mentioned above, the integral mode of the detector is needed during periods of high SEP fluxes. As an example of data processing, we can take one of the SEP events from [12]. The expected spectrum of protons is presented in figure 17.

The passage of particles through the detector matter is simulated using Geant4. Detector model consisted of 100 disks 1 millimeter thick. To bring the detector model closer to the real prototype, the energy deposition in each of four adjacent disks was summed up, so we have 25 washes 4 millimeters thin. Protons pass perpendicular to the detector disks, their energy ranges from 1 to 150 MeV.

Turchin algorithm was applied in Julia and Python programming languages. Python package was applied to Nu-Mass data analysis [13]. Package [TurchinReg.jl](#) allows to use different bases

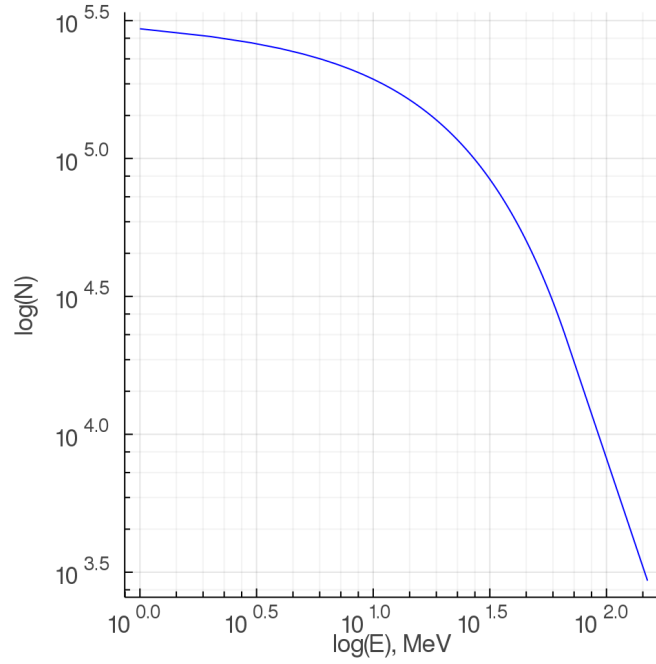


Figure 17: The expected spectrum.

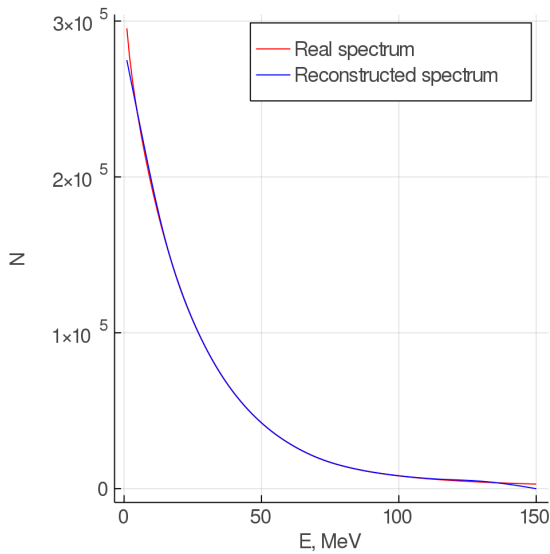


Figure 18: Reconstruction of protons spectrum (100 disks 1mm thick).

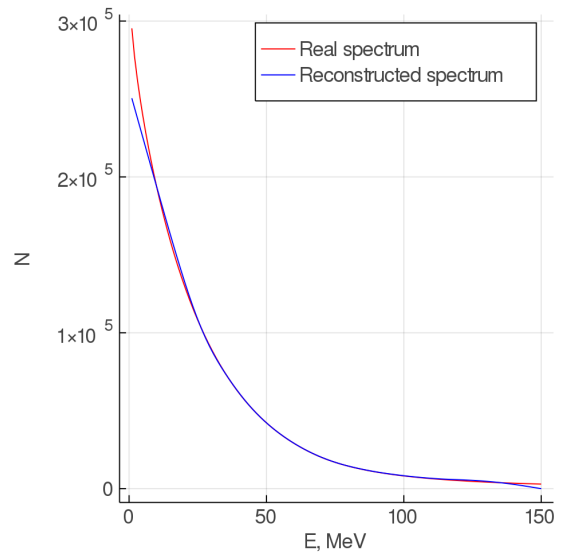


Figure 19: Reconstruction of protons spectrum (25 disks 4mm thick).

and regularisation parameters. The result of data processing is presented in figures 18, 19. The average relative accuracy of spectrum reconstruction using the Turchin algorithm is about 7%. As a result, even some washes have bad resolution, it is possible to reconstruct the spectrum using Turchin regularisation algorithm.

The integral mode analysis was currently focused only on proton spectrum reconstruction because the lack of experimental data with electrons. The preliminary study shows that it is possible to reconstruct both electron and proton spectra simultaneously with only minor loss for precision, but it requires additional study.

8 Conclusion

The detector prototype presented in this article has several key features:

- Its construction is simple and it has small mass. What is more important is that it does not require heavy shielding and collimators and effectively uses almost all its mass.
- The material of the detector is solid plastic, which makes it less susceptible to radiation and thermal damage, than semi-conductor detectors and less fragile than gas detectors.
- The segmentation allows to significantly improve energy resolution in differential (individual event) measurement mode. The detection energy threshold could be adjusted by turning off frontal detector segments and thus allowing to use differential mode measurements even during solar events, when the count rate is really high.
- Another benefit of segmentation is an ability to use integral (spectral measurement) mode in case of very high count rates ($\sim 10^7$ Hz and even higher), while limiting the amount of computation time and data transmission rates.
- Integral mode analysis is supplemented by unique implementation of Turchin's statistical regularization algorithm for spectrum reconstruction.

Laboratory tests and simulations results show its suitability for spectroscopy of selected particles. Despite relatively poor energy resolution of detector segments themselves, the profile reconstruction from all segments gives better than 5% relative precision for protons and electrons in differential mode. Turchin's regularisation allows proton spectrum restoration with better than 7% accuracy. Simultaneous reconstruction with electrons requires additional study, but we do not expect the worst accuracy to drop below 10%.

In future, it is planned to develop new electronics suitable for detector operation in space. Moreover, detector design will be adjusted to spacecraft requirements, e.g. minimization of mass-size characteristics, side shielding etc.

This work is supported by the Russian Science Foundation under grant No. 17-72-20134.

References

- [1] <https://www.dupont.com/brands/tyvek.html>.
- [2] <https://hamamatsu.su/>.
- [3] D. N. Baker, X. Li, N. Turner, J. H. Allen, L. F. Bargatze, J. B. Blake, R. B. Sheldon, H. E. Spence, R. D. Belian, G. D. Reeves, S. G. Kanekal, B. Klecker, R. P. Lepping, K. Ogilvie, R. A. Mewaldt, T. Onsager, H. J. Singer, and G. Rostoker. Recurrent geomagnetic storms and relativistic electron enhancements in the outer magnetosphere: ISTP coordinated measurements. *JGR*, 102(A7):14141–14148, July 1997.

- [4] P. Buzhan, B. Dolgoshein, L. Filatov, A. Ilyin, V. Kantzerov, V. Kaplin, A. Karakash, F. Kayumov, S. Klemin, E. Popova, and S. Smirnov. Silicon photomultiplier and its possible applications. *Nuclear Instruments and Methods in Physics Research A*, 504(1-3):48–52, May 2003.
- [5] B. Dolgoshein, V. Balagura, P. Buzhan, M. Danilov, L. Filatov, E. Garutti, M. Groll, A. Ilyin, V. Kantserov, V. Kaplin, A. Karakash, F. Kayumov, S. Klemin, V. Korbel, H. Meyer, R. Mizuk, V. Morgunov, E. Novikov, P. Pakhlov, E. Popova, V. Rusinov, F. Sefkow, E. Tarkovsky, I. Tikhomirov, and Calice/SiPM Collaboration. Status report on silicon photomultiplier development and its applications. *Nuclear Instruments and Methods in Physics Research A*, 563(2):368–376, July 2006.
- [6] Turchin V. F. Solution of the fredholm equation of the first kind in a statistical ensemble of smooth functions. *Journal of Computational Mathematics and Mathematical Physics*, 6, 1967.
- [7] Turchin V. F. and Nozik V. Z. Statistical regularization of solving ill-posed problems. *Physics of the atmosphere and the ocean*, 1969.
- [8] M. B. Kallenrode. Current views on impulsive and gradual solar energetic particle events. *Journal of Physics G Nuclear Physics*, 29(5):965–981, May 2003.
- [9] Shu T. Lai. *Fundamentals of Spacecraft Charging*. 2011.
- [10] Olga E. Malandraki and Norma B. Crosby. *Solar Energetic Particles and Space Weather: Science and Applications*, volume 444 of *Astrophysics and Space Science Library*, pages 1–26. 2018.
- [11] D. J. McComas, N. Alexander, N. Angold, S. Bale, C. Beebe, B. Birdwell, M. Boyle, J. M. Burgum, J. A. Burnham, E. R. Christian, W. R. Cook, S. A. Cooper, A. C. Cummings, A. J. Davis, M. I. Desai, J. Dickinson, G. Dirks, D. H. Do, N. Fox, J. Giacalone, R. E. Gold, R. S. Gurnee, J. R. Hayes, M. E. Hill, J. C. Kasper, B. Kecman, J. Klemic, S. M. Krimigis, A. W. Labrador, R. S. Layman, R. A. Leske, S. Livi, W. H. Matthaeus, R. L. McNutt, R. A. Mewaldt, D. G. Mitchell, K. S. Nelson, C. Parker, J. S. Rankin, E. C. Roelof, N. A. Schwadron, H. Seifert, S. Shuman, M. R. Stokes, E. C. Stone, J. D. Vande-griff, M. Velli, T. T. von Rosenvinge, S. E. Weidner, M. E. Wiedenbeck, and P. Wilson. Integrated Science Investigation of the Sun (ISIS): Design of the Energetic Particle Investigation. *SSR*, 204(1-4):187–256, December 2016.
- [12] R. A. Mewaldt, C. M. S. Cohen, A. W. Labrador, R. A. Leske, G. M. Mason, M. I. Desai, M. D. Looper, J. E. Mazur, R. S. Selesnick, and D. K. Haggerty. Proton, helium, and electron spectra during the large solar particle events of october–november 2003. *Journal of geophysical research*, 2005.
- [13] Alexander Nozik Alexey Khudyakov Mikhail Zelenyi, Mariia Poliakova. Application of turchin’s method of statistical regularization. *The XXI International Scientific Conference of Young Scientists and Specialists (AYSS-2017)*, 2017.
- [14] L. I. Miroshnichenko. Solar cosmic rays: 75 years of research. *Physics Uspekhi*, 61(4):323–352, April 2018.
- [15] Leonty Miroshnichenko. *Solar Cosmic Rays*, volume 405. 2015.
- [16] Arik Posner. Up to 1-hour forecasting of radiation hazards from solar energetic ion events with relativistic electrons. *Space Weather*, 5(5):05001, May 2007.
- [17] Donald V. Reames. The Two Sources of Solar Energetic Particles. *SSR*, 175(1-4):53–92, June 2013.
- [18] Rodriguez-Pacheco, J., Wimmer-Schweingruber, R. F., Mason, G. M., Ho, G. C., Sánchez-Prieto, S., Prieto, M., and et al. The energetic particle detector. energetic particle instrument suite for the solar orbiter mission. *A&A*, 2019.
- [19] A. B. Struminskii, I. Yu. Grigor’eva, Yu. I. Logachev, and A. M. Sadovskii. Solar Electrons and

Protons in the Events of September 4-10, 2017 and Related Phenomena. *Plasma Physics Reports*, 46(2):174–188, March 2020.

- [20] A. B. Struminsky. Solar Proton Events of September 6 and 10, 2017: Moments of the First Arrival of Protons and Electrons. *Bulletin of the Russian Academy of Sciences, Physics*, 83(5):538–542, May 2019.
- [21] Martin Wuest, David S. Evans, James P. McFadden, Wayne T. Kasprzak, Larry H. Brace, Bronislaw K. Dichter, Walter R. Hoegy, Alan J. Lazarus, Arnaud Masson, and Oleg Vaisberg. Review of Instruments. *ISSI Scientific Reports Series*, 7:11–116, January 2007.
- [22] M. E. Zelenyi, E. M. Stadnichuk, A. A. Nozik, I. V. Zimovec, A. G. Kudinov, and I. K. Reznikov. Designing proton and electron detector for monitoring solar cosmic rays. *Bulletin of the Lebedev Physics Institute*, 46(1):23–25, 2019.

Appendix

Muon signal distribution

Assumptions

1. The distribution of muons by the angle of incidence on the scintillator disk is $f(\theta) = \cos^2\theta$ with $\theta \in [0, \frac{\pi}{2}]$
2. Muons always fly through the top and the bottom of the disk or through both sides of the disk.
3. Error for the fixed signal has normal distribution, but sigma depends on the value of the signal.
4. Disk light collection heterogeneity is ignored.

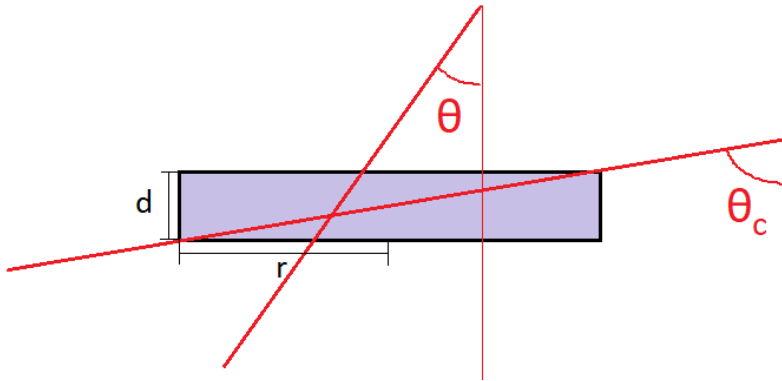


Figure 20: Muon propagation through detector channel scheme.

Muon energy deposition

One channel of the detector is a scintillator disk with cylinder shape. The disk is made out of polystyrene. Its radius is $r = 3$ cm and it's width is $d = 0.4$ cm.

When a muon propagates through the disk perpendicular to the top surface disk it loses $\varepsilon_0 = 1.02$ MeV within the scintillator. Muons are MIPs (Minimum Ionizing Particles), consequently, if a muon propagates through a layer of scintillator with length $= l$, then it loses $\varepsilon_0 \cdot \frac{l}{d}$ of its energy.

Muon propagates through the disk diagonal when its angle of incidence is equal to $\theta_c = \arccos(\frac{d}{2r}) \approx 1.44$ radian (figure 20). This angle further will be called the critical angle. If muon's angle of incidence is less than θ_c then under made assumptions it will cross the disk through the top and the bottom surfaces. So its energy deposit can be found in the following way:

$$\varepsilon(\theta) = \frac{\varepsilon_0}{\cos \theta} \quad (8.1)$$

If muon's angle of incidence is more than θ_c then the muon propagates through size surface of the disk. Consequently, its energy deposit can be estimated in the following way:

$$\varepsilon(\theta) = \varepsilon_0 \frac{2r}{d \sin \theta} \quad (8.2)$$

Minimum muon energy deposit is equal to $\varepsilon(0) = \varepsilon_0 = 1.02$ MeV. Maximum muon energy deposit is equal to $\varepsilon_c = \varepsilon(\theta_c) \approx 7.72$ MeV. And the general formula looks as follows:

$$\varepsilon(\theta) = \begin{cases} \frac{\varepsilon_0}{\cos \theta} & \theta \leq \theta_c \\ \varepsilon_0 \frac{2r}{d \sin \theta} & \theta \geq \theta_c \end{cases}$$

Muon energy deposit distribution

Let muon angle distribution be $f(\theta) = \cos^2 \theta$. Let muon energy deposit in the channel distribution be $f(\varepsilon)$. Considering ε being monosemantic function of θ the following equation takes place:

$$f(\theta)d\theta = f(\varepsilon)d\varepsilon = f(\varepsilon)\frac{d\varepsilon}{d\theta}d\theta \quad (8.3)$$

$\varepsilon(\theta)$ consists of two parts. If $\theta \leq \theta_c$, then

$$f(\varepsilon)\frac{d\varepsilon}{d\theta}d\theta = f(\varepsilon)\varepsilon_0 \frac{\sin \theta}{\cos^2 \theta}d\theta = f(\theta)d\theta \quad (8.4)$$

Consequently,

$$f(\varepsilon) = f_0 \cdot \cos^2 \theta \cdot \frac{\cos^2 \theta}{\varepsilon_0 \sin \theta} = f_0 \frac{\varepsilon_0^3}{\varepsilon^4 \sqrt{1 - (\frac{\varepsilon_0}{\varepsilon})^2}} \quad (8.5)$$

Here f_0 is a normalization coefficient. Similarly for $\theta > \theta_c$ the distribution is as follows:

$$f(\varepsilon) = f_0 \cos^2(\theta) \frac{\sin^2 \theta}{\varepsilon_0 \cos \theta} = f_0 \varepsilon_0 \left(\frac{2r}{\varepsilon d} \right)^2 \sqrt{1 - \left(\frac{2r \varepsilon_0}{\varepsilon d} \right)^2} \quad (8.6)$$

Denoting $\varepsilon(\theta_c)$ as ε_c , the normalization coefficient is sought via following formula:

$$f_0 = \frac{1}{\int_{\varepsilon_0}^{\varepsilon_c} \frac{\varepsilon_0^3}{\varepsilon^4 \sqrt{1 - (\frac{\varepsilon_0}{\varepsilon})^2}} d\varepsilon + \int_{\varepsilon(\frac{\pi}{2})}^{\varepsilon_c} \varepsilon_0 \left(\frac{2r}{\varepsilon d} \right)^2 \sqrt{1 - \left(\frac{2r\varepsilon_0}{\varepsilon d} \right)^2} d\varepsilon} \quad (8.7)$$

$\varepsilon(\frac{\pi}{2}) \approx 7.65 \text{ MeV} < \varepsilon_c$. Consequently, for $\varepsilon \in (7.65 \text{ MeV}, 7.72 \text{ MeV})$ the total distribution is a sum of distributions for both considered cases. Therefore, muon energy deposit distribution is as follows (figure 21):

$$f(\varepsilon) = \begin{cases} f_0 \cdot \cos^2 \theta \cdot \frac{\cos^2 \theta}{\varepsilon_0 \sin \theta} = f_0 \frac{\varepsilon_0^3}{\varepsilon^4 \sqrt{1 - (\frac{\varepsilon_0}{\varepsilon})^2}} & \varepsilon < 7.65 \text{ MeV} \\ f_0 \cos^2(\theta) \frac{\sin^2 \theta}{\varepsilon_0 \cos \theta} = f_0 \varepsilon_0 \left(\frac{2r}{\varepsilon d} \right)^2 \sqrt{1 - \left(\frac{2r\varepsilon_0}{\varepsilon d} \right)^2} & \varepsilon \in (7.65 \text{ MeV}, 7.72 \text{ MeV}) \end{cases}$$

$$f_0 = \frac{1}{\frac{1}{4} \sin(2 \arccos(\frac{\varepsilon_0}{\varepsilon})) \Big|_{\varepsilon_0}^{\varepsilon_c} + \frac{\arccos(\frac{\varepsilon_0}{\varepsilon})}{2} \Big|_{\varepsilon_0}^{\varepsilon_c} + \frac{r}{d} \arccos(\frac{\varepsilon_0}{\varepsilon}) \Big|_{\varepsilon(\frac{\pi}{2})}^{\varepsilon_c} - \frac{r}{2d} \sin(2 \arccos(\frac{\varepsilon_0}{\varepsilon})) \Big|_{\varepsilon(\frac{\pi}{2})}^{\varepsilon_c}} \quad (8.8)$$

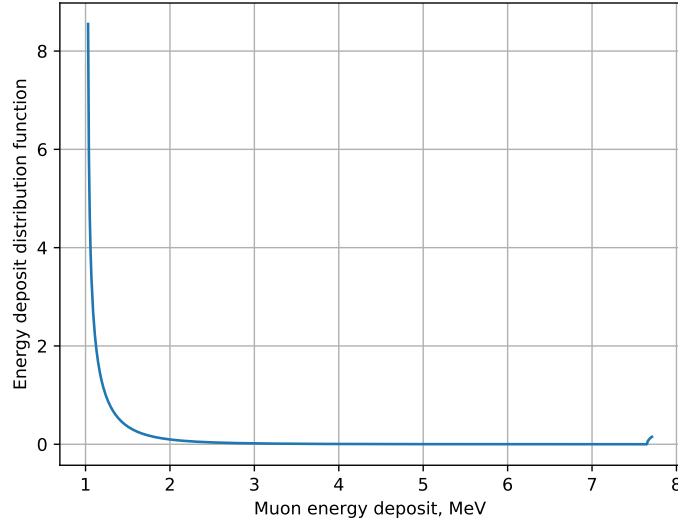


Figure 21: Muon energy deposit within a detector channel distribution.

Muon signal distribution

If a detector channel is irradiated with a monochromatic particle beam then every particle from this beam will deposit the same energy within the channel. But the signal, obviously, will have a normal distribution due to detector channel error. Also it is a well-known fact that scintillator detectors' errors are root-dependent on the energy deposit. Consequently, muon signal distribution is sought from the following convolution (figure 22):

$$F(\varepsilon) = \int_0^{\varepsilon_c} f(E)N(\varepsilon - E, \sigma\sqrt{\varepsilon})dE \quad (8.9)$$

Here σ is a coefficient in the error root-dependence. Its physical meaning - detector channel error for 1 MeV energy deposit detection. Further this coefficient will simply be called channel error.

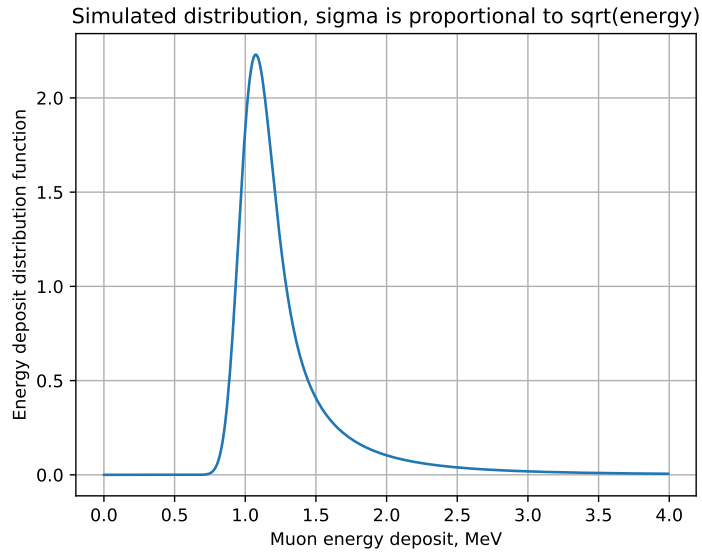


Figure 22: Example of theoretical muon signal distribution with good detector resolution.